The Dust Environment of Comet Siding Spring at Mars

Report on the Hazards to Mars Orbiting Spacecraft due to Cometary Dust

Tony L. Farnham, Michael S.P. Kelley, Dennis Bodewits
University of Maryland
24 April 2014

Summary

On October 19, 2014, just 6 days before its perihelion at 1.4 AU, comet Siding Spring (C/2013 A1) will have a close encounter with Mars. The comet will approach to within 135,000±5000 km at 18:29 UTC (±3 min) (JPL Orbital Solution #46). During this event, the planet may pass through the dust surrounding or trailing behind the comet, presenting a potential hazard to the spacecraft in orbit around Mars, especially given the high relative velocity of 56 km/s. We used observations of the comet to characterize its dust properties and activity levels since discovery. With this information, we developed a model of the comet, which we then used to simulate what the dust environment will be like at the time around the close approach to Mars.

Results from these simulations indicate that Siding Spring's dust emission velocities are low enough that solar radiation pressure tends to sweep the dust grains down the tail before they have the chance to reach Mars. For our nominal comet model, we see no impacts at Mars. For our worst-case scenario model (which includes the ephemeris uncertainty), we do see impacts, but the fluences are very low, with a peak around 4×10^{-7} grains/m^2, consisting of grains ~0.5 to 3 mm in diameter. The time of arrival for these grains spans 88 to 108 minutes after the time of closest approach, when Mars is closest to the comet's orbit. These results suggest that hazards to the orbiting spacecraft will be minimal, especially when compared to the background impact flux, which is ~3 orders of magnitude higher over the 5 year mission.

Contents

1 Comet Physics

2 Characterization of Comet Properties
2.1 Observations
2.2 Onset of Activity and General Activity Trends
2.3 Gas Production
2.4 Dust Production
2.5 Maximum Dust Grain Size
2.6 Dust Emission Velocities
2.7 Particle Size Distribution
2.8 Dust Tail Modeling
2.9 Nominal Siding Spring Model

3 Dust Hazard Analysis
3.1 Dust Dynamics
3.2 Reference Frames
3.3 Dust Coma Simulations
3.4 Impact Criteria
3.5 Simulation results
3.6 Impact Hazard

4 Comparison to Other Results

1 Comet Physics

A comet's nucleus is comprised of ices (volatiles) and dust. When it approaches the Sun, the ices begin to vaporize and gas (primarily CO, CO_2 and H_2O) streams out into space. As the gas leaves the nucleus, it transfers momentum to the dust, lifting grains off the surface and accelerating them out into the comet's coma. As the heliocentric distance decreases, the increase in solar energy means that more gas is produced, which in turn increases the amount of dust that can be ejected, as well as increasing the emission velocity that the dust can attain.

After a particle has left the microgravity environment at the nucleus, the primary forces it experiences are solar gravity (which wants to keep it in a solar orbit) and solar radiation pressure (which wants to push it away from the Sun). The effects of radiation pressure are proportional to a grain's cross sectional area and inversely proportional to its mass, so small grains are accelerated more rapidly than larger ones. These differential forces effectively "sort" the grains into different regions of the tail, which straddles the comet's orbital plane. A more detailed discussion of the dust dynamics will be presented in the description of our simulations in Section 3.

2 Characterization of the Comet Properties

In order to predict what the dust environment will be like at the time of the Mars encounter, we must determine or assume the basic properties of the comet and use those properties to model its behavior as a function of time.

Specific items of interest, and how they factor into the analysis, include:

1) *The onset of activity*. Dust emitted at very large heliocentric distances requires a lower emission velocity to reach Mars. The earlier the activity starts, the smaller velocities that are required to allow the dust to reach Mars (e.g. Farnocchia et al. 2014).

2) *Gas production rate*. Controls the amount of dust that can be lifted off the surface (including the largest size of a single grain that can leave the surface), and the velocity to which the particles can be accelerated. The gas production can also be used to constrain the total amount of dust that is emitted from the nucleus.

3) *Dust production rate*. Defines how much dust is leaving the comet and is available for impacts around Mars. As described below, measurements are typically obtained as the somewhat cryptic parameter, $A(\theta)f\rho$, which is converted to a mass production rate via the particle size distribution, expansion speeds and albedo.

4) *Dust emission speed*. Defines how fast the grains leave the nucleus. For a given grain size, a specific range of emission speeds are required to reach Mars.

5) *Dust particle size distribution (PSD)*. Defines how the dust sizes are distributed, with most comets having many very small grains and only a relatively few large ones. For the Mars hazard analysis, the concern is for grains in the size range ~50 μm to ~0.5 cm (though our simulations include grains outside this range as well).

2.1 Observations

Due to the faintness of the comet and the difficulty of obtaining ground-based observations, the data available for characterizing the comet are somewhat limited. Most of our information comes from spacecraft observations (HST, NEOWISE and Swift). Table I lists the primary observations that were used in this study, with basic geometric information and results.

The HST/WFC3 data consist of two-color (438 and 606 nm) imaging, providing high resolution pictures of the coma morphology. These images can be used to measure the dust velocities and production rates (Afρ, A'Hearn et al., 1984), as well as revealing any detailed structure in the inner comae. The spatial structure of the dust in the tail also acts as the input constraint for our Finson-Probstein models that derive the dust properties, as described in Section 2.8. The NEOWISE and Spitzer data both consist of two-filter images (3.6 and 4.5 μm), which can be used for estimating Afρ as well as providing constraints on the CO_2 (or CO) gas production. The Swift/UVOT measurements consist of images at 260 and 547 nm, providing measurements of Afρ and OH production (which is used for deriving the water production rate).

Table I. Siding Spring Observational Data

Date	r_h [1] (AU)	Δ [2] (AU)	α [3] (deg)	A(0)fρ [4] (cm)	Comments [5]
PanSTARRS					
20 Nov 2011	10.3	9.6	4		Undetected
2 Dec 2011	10.2	9.5	4		Undetected
HST/WFC3					
29 Oct 2013	4.6	4.0	11	2705	
21 Jan 2014	3.8	3.7	15	2365	
11 Mar 2014	3.3	3.8	14	1920	
NEOWISE					
16 Jan 2014	3.8	3.7	15	280	$Q(CO_2) = 4\times10^{26}$
Swift/UVOT					
2 Nov 2013	4.5	4.0	11	1740	$Q(H_2O) < 6\times10^{27}$
28 Dec 2013	4.0	3.6	14	1495	$Q(H_2O) < 2\times10^{27}$
18 Feb 2014	3.5	3.8	15	1530	$Q(H_2O) < 3\times10^{27}$
15 Mar 2014	3.2	3.8	14	1100	$Q(H_2O) < 3\times10^{27}$
Spitzer					
26 Mar 2014	3.1	3.1	19	1460	$Q(CO_2) = 3.5\times10^{26}$

[1] Heliocentric distance
[2] Geocentric distance or Spacecraft range
[3] Solar phase angle
[4] A measure of dust in the coma
[5] Q = gas production (molecules/sec)

In the following sections we will present various techniques that are used to determine the properties necessary to constrain our simulations. These techniques range from simple calculations of a single value, to more elaborate models that attempt to derive a more comprehensive solution involving multiple comet properties.

2.2 Onset of Activity and General Activity Trends

Comet Siding Spring was discovered on 3 January 2013, at a heliocentric distance, r_h, of 7.2 AU, at which time the nucleus was clearly active. Prediscovery images were subsequently found from as early as 4 October 2012, indicating that activity had already begun by 7.9 AU. To determine if it was active prior to this time, we requested a search of two different wide-field camera databases (CFHT's MegaCAM and the PanSTARRS NEO search database), to look for even earlier images. This search, performed by Jan Kleyna at the University of Hawaii, turned up four additional images from November and December 2011 (r_h from 10.3 to 10.2 AU) that fortuitously captured the region of the sky containing Siding Spring (as predicted by the ephemeris). There was no sign of the comet in any of these images, nor was it visible when relevant frames were coadded to improve the signal-to-noise. The absence of a detection in December 2011, to a 5-σ limit of 23rd mag, puts a severe constraint on the brightness of Siding Spring at 10.2 AU. This in turn suggests that

the comet's activity ramped up at some point between 10 and 8 AU. The onset of activity will be discussed further with regards to the dust tail modeling in Section 2.8.

Figure 1 shows a compilation of the Siding Spring's photometric brightness and Afρ as a function of heliocentric distance, reflecting its activity level as a function of time. If we only consider the direct detections (from 8 to 3 AU), then the activity appears to increase as r_h^{-3} beyond 6 AU. If this relation were accurate, then the comet should have easily been detected in the measurements from 10 AU. Because it was not seen, we can constrain the trend analysis with the non-detections, which suggest the brightness initially increases much more steeply (as $\sim r_h^{-7}$). Although the actual behavior could vary somewhat (e.g., steeper than r_h^{-7} up to 8 AU, then r_h^{-3}), this result provides us with a strong argument that the comet was exhibiting little activity at 10 AU, providing a limit for the emission times that must be considered in our simulations.

Also seen in Figure 1 is a flattening of the profile, where the brightness remains essentially constant between 6 and 3 AU. This behavior is typical of dynamically new comets (Oort & Schmidt 1951), and reflects the early emission and subsequent depletion of highly volatile ices (Whipple 1978), before the activity begins to ramp up again around 3 AU. Unfortunately the comet moved into solar conjunction at ~3 AU, so no observations are yet available to address this range.

2.3 Gas Production

The Swift observations in the OH filter (e.g., Bodewits et al. 2014) provide constraints on the water production (OH is a photodissociation product of water). None of the four observations available through March 2014 detected any OH. This allows us to put 3-σ upper limits on the water production rate, as listed in Table I. As of March 2014, the water production was $<3\times10^{27}$ molecules/s, confirming the result from the photometry that activity is still low at ~3 AU.

Given this limit, it is possible that water could be contributing $\sim10^{27}$ molecules/sec at $r_h = 3$ AU, but this production rate will fall off dramatically for $r_h > 4$ AU where temperatures are too cold for significant water sublimation (Ootsubo et al. 2012). As will be seen in Section 4.3, dust that poses a hazard during the Mars encounter must leave the comet before the nucleus reaches ~4.5 AU, so water production will not play a significant role in the production of hazardous dust.

Gas detections were obtained from both the NEOWISE observations from 21 Jan 2014, (Stevenson & Bauer, private communication) and the Spitzer observations from 26 March 2014, using measurements at 3.6 and 4.5 μm. A solar reflectance spectrum is fit through 3.6 μm measurement and projected out to 4.5 μm. If the 4.5 μm point lies well above the projected value, then it is assumed that the excess is due to gas bands within the filter. The excess could be due to either CO or CO_2, as both have significantly strong emission bands within the filter bandpass (Crovisier & Encrenaz 1983). As discussed below, we believe that the excess in Siding Spring is primarily due to CO_2, which gives production rates of $Q(CO_2) = 4\times10^{26}$ molecules/sec for the NEOWISE data and 3.5×10^{26} molecules/sec for the Spitzer data. This is further evidence that the comet's activity was flat during this time.

We argue that the excess signal comes primarily from CO_2, for three reasons: First, CO has a very low sublimation temperature, and if it were present in large amounts, the comet should exhibit a relatively constant production rate, starting at very large heliocentric distances (>15 AU). CO_2, on the other hand, has a higher sublimation temperature, and it should start to ramp up inside of 13 AU (Meech & Svoren 2004), which is what is observed. Second, the fluorescence efficiencies of CO_2 are larger than those of CO, so the amount of CO necessary to produce the observed signal (~$4.\times10^{27}$ molecules/sec or ~220 kg/sec) would be ~10 times that for CO_2 (4×10^{26} molecules/sec or ~30 kg/sec). If the dust-to-gas ratio is assumed to be 1 (a nominal value for comet coma), then the mass loss for CO_2 is more consistent with our other estimates of the dust production (discussed below) than for CO. (This does not preclude the excess being due to CO, but if so, then the dust-to-gas ratio would need to be significantly less than 1.) Third, observations suggest that for comets at $r_h < 4$ AU, the production rate of CO_2 is equal to or greater than the production rate of CO (Ootsubo et al. 2012), which would indicate that the majority of the 4.5 μm excess would arise from CO_2.

Thus, we adopt the gas production of $Q(CO_2) = 4\times10^{26}$ (30 kg/sec) at 3.8 AU as a basic result from the NEOWISE and Spitzer observations.

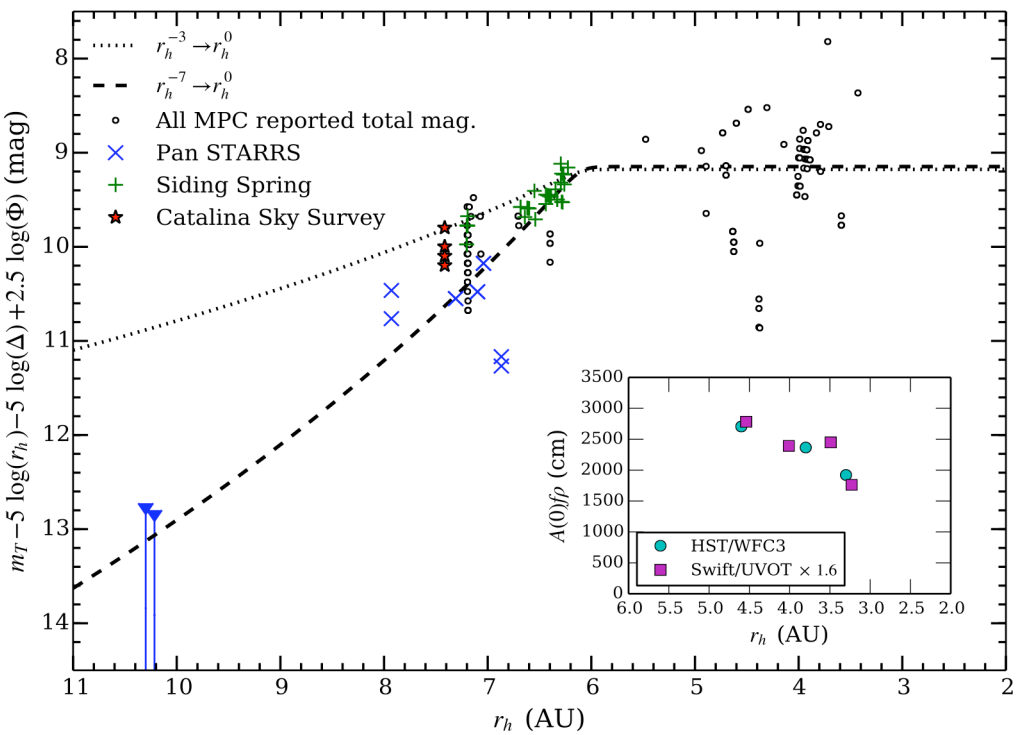

Figure 1. Compilation of photometry and Afρ measurements for comet Siding Spring between 10.3 and 3.0 AU. The left scale shows the comet's absolute magnitude, while the inset gives Afρ for the HST and Swift observations. The upper magnitude limits to the left represent the prediscovery fields where the comet is not detected, suggesting that there was a steep increase in brightness between 10 and 8 AU. From 6 to 3 AU, the brightness flattened somewhat, which is not unusual for dynamically new comets. The trend lines depict the general behavior if the non-detections are included (dashed line) as well as an envelope for measurements only out to 8 AU (dotted line).

2.4 Dust Production

The most straightforward technique we have for estimating the dust mass loss rate is to adopt a dust-to-gas ratio and compute it directly from the gas production. Assuming the dust-to-gas ratio is 1 (a typical assumption for comets), then the mass production of dust, based on the CO_2 production is ~30 kg/sec at 3.8 AU

Another technique is to use the $Af\rho$ values listed in Table I. $Af\rho$ is a measure of the brightness of dust within a given aperture (A'Hearn et al. 1984), but if we make some assumptions about the albedo, scattering properties, and density of the dust grains, and adopt the dust emission velocity and size distributions derived below, we can use $Af\rho$ to estimate the mass production rate. For a nominal geometric albedo of 0.05, scattering efficiency Q_{sca}=1, and a grain density of 1 g/cm^3, the dust production rate for the HST measurements corresponds to a dust mass of ~7-9 kg/sec for the October, January and March observations, reinforcing the conclusion that the activity stayed flat through this period. Similarly, $Af\rho$ from the NEOWISE and Spitzer observations gives mass losses of ~30 kg/sec and 26 kg/sec, respectively. A final measure of the dust production comes from the dust tail modeling in Section 2.8, giving a value in the range 15-18 kg/sec.

The various measurements from the different techniques range from 7-30 kg/sec. Given this result, we adopt a value of 30 kg/sec at 3.8 AU as our nominal mass loss rate for the hazard analysis simulations. As the highest value, this provides a conservative estimate of the dust production.

2.5 Maximum Dust Grain Size

The maximum ejected grain radius, a_{crit}, is a function of the amount of gas available for lifting a given mass off the surface and accelerating it to escape velocity. Thus, a_{crit}, is directly proportional to the production rate and molecular mass of the driving gas. For the CO_2 production rate of 4×10^{26} molecules/sec, and assuming a grain density of 1 g/cm^3, a nucleus density of 0.3 g/cm^3, and a nucleus radius of 2 km (consistent with the CO_2 production rate), we compute a value a_{crit} = 100 μm at r_h = 8 AU (Meech & Svoren 2004). Note that a_{crit} should only be considered an order of magnitude estimate because of the various assumptions and unknowns. For example, it depends inversely on the nucleus radius to the 3rd power, so a nucleus twice as large will have an a_{crit} that is almost an order of magnitude smaller (or an order of magnitude larger for a nucleus half the size).

2.6 Dust Emission Velocities

The dust emission velocity is a critical parameter for the simulations, because it controls the distance from the nucleus that the dust can attain, and thus is important in determining if the grains will reach Mars. (In the following, the term "emission velocity" refers to the velocity of the grain after it has escaped the nucleus' gravitational pull and is outside the collision zone of the gas coma.) Theoretical computations based on hydrodynamic arguments suggest that the velocity follows a relation $v \sim v_0\, a^{-0.5}\, r_h^{-1.0}$, where v_0 is the emission velocity of a 1 μm grain at 1 AU (Whipple 1951, Tricarico et al. 2014).

Deviations from this function are common and reflect the complexities of the hydrodynamics that form the comet's coma. Thus, qualitative measurements are desired to provide the best values possible for constraining our simulations.

One technique we used to constrain the velocity is based on the standoff distance of the coma in the sunward direction. Grains emitted in the sunward direction will initially move outward with their typical emission velocity. The acceleration of radiation pressure will cause them to slow and eventually stop and turn around, to then be pushed back into the dust tail. Since the acceleration can be computed for a particular grain size, it is possible to use the point at which it turns around to derive the initial velocity. This "standoff distance" is usually well defined on the sunward side of a comet, so this is a simple and straightforward technique for constraining the maximum velocity of the dust. Because small grains are the most efficient at scattering light, we assume that small grains (~1 μm) are defining the standoff distance, and extrapolate velocities to larger grains using assumed or derived functions.

Using the high-resolution HST images, we derive velocities for the three HST epochs of 27, 43 and 54 m/sec for 1 μm grains. Taken by themselves, these velocities suggest that the dependence of velocity on heliocentric distance goes as $\sim r_h^{-2}$ which is steeper than the theoretical value, but not unphysical. The impact of this dependence is that particles would attain significantly higher velocities when the nucleus is close to the Sun than they would for the theoretical case, while having slightly lower velocities at large distances. This suggests we should explore this scenario in our simulations to see if the small, fast moving particles emitted later in the apparition, should be a concern. Figure 2 shows a plot of the measurements with different power law fits overlaid. Given the uncertainties and assumptions involved, we cannot exclude the shallower functions.

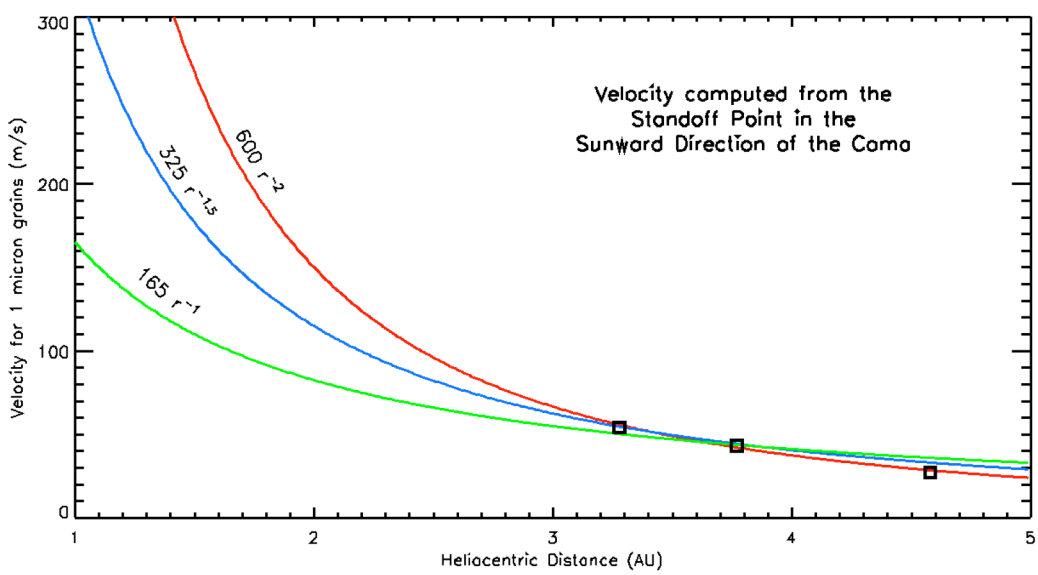

Figure 2. Plot showing dust velocities for grains of 1 μm radius as a function of heliocentric distance. The points show data measured using the standoff distances in the HST data at three epochs, and the curves are the best fits for three power law functions.

An additional derivation of dust velocities, from the dust tail modeling, is discussed in section 2.8.

2.7 Particle Size Distribution

Direct measurements of the particle size distribution are difficult to obtain. Size distributions, dn/da, that have been measured, can usually be expressed as power law functions of a, with exponents between -3 and -5 (Fulle et al. 2004). In the absence of additional information, typical distributions are assumed to follow an a^{-4} relation. This parameter will be addressed further in the next section.

2.8 Dust Tail Modeling

The final tool that we utilized in our characterization of the comet was modeling of the dust tail using a modified Finson-Probstein (F-P) technique (Finson & Probstein 1968) as developed by Farnham (1996). F-P modeling relies on the process in which dust grains of different sizes are sorted into predictable regions of the tail by the actions of radiation pressure. "Maps" of the syndynes (loci of the positions of test particles of a single size, emitted over time) and synchrones (loci of the positions of test particles of all sizes, emitted at one time) show the regions of the tail where grains of a particular size, emitted at a particular time, should be centered. With these maps, it is possible to model the brightness distribution of the tail, and to determine the properties of the dust in the process. The top row in Figure 3 shows the HST images, with syndynes and synchrones overlaid, that were used with this technique.

Parameters that are constrained using these models are 1) the particle size distribution, assumed to follow a power law dependence, $dn/da \sim a^X$; 2) the dust production rate as a function of time, which is represented by values at discrete points in time, with linear interpolations between them; 3) the dust velocity, assumed to follow the relation $v \sim v_0\, a^Y\, r_h^Z$.

The modeling is done in a stepwise manner, by assigning values to the dust parameters and using them to generate a model of the dust distribution in the tail. (We adopted the values discussed in previous sections as our initial parameter set.) The model is then compared to the observed image and, using the syndynes and synchrones as a guide, the parameters are modified to adjust the brightness distribution, in and attempt to improve the results. This iterative process proceeds until satisfactory fits to the data are obtained.

The advantage of the full tail model over the previous determinations is that it attempts to incorporate a broader range of grain sizes and emission times, with the spatial distribution providing the constraints. The modeling also produces a bigger set of dust properties that are self-consistent in scope. The drawback of the modeling is that it relies on a number of assumptions and simplifications that may affect the results, and solutions can vary somewhat due to violations of those assumptions. The use of several images, from different times, alleviates some of these concerns, because much of the same dust is present in all of the images, moving from one time to another, and one set of parameters must be found to match all images.

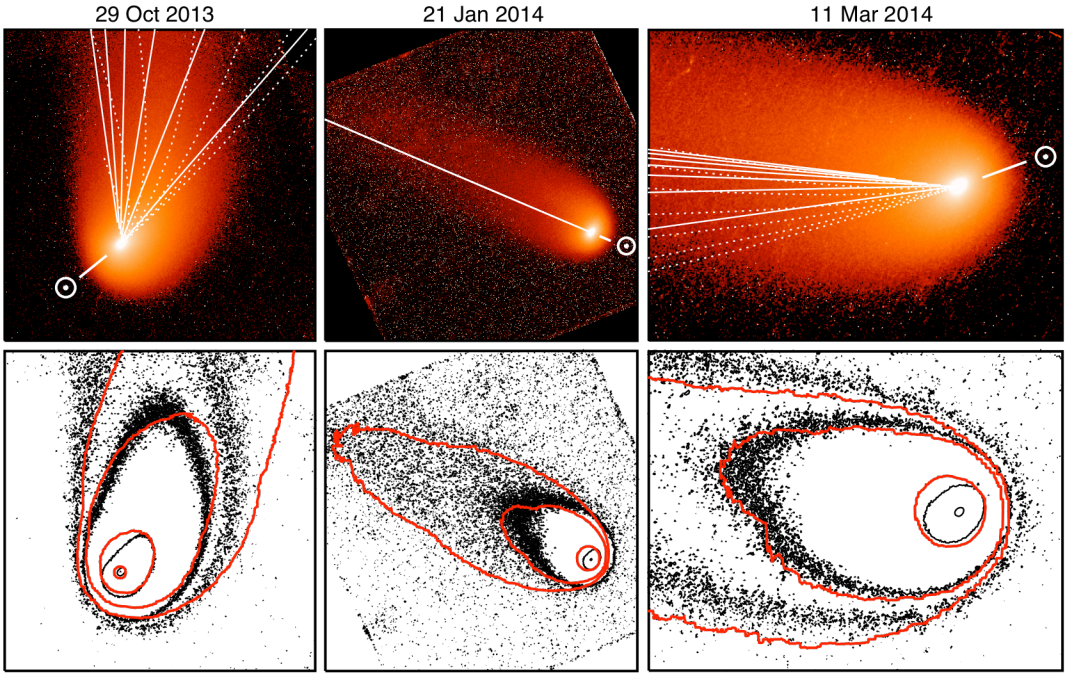

Figure 3. Top Row: HST images modeled using the F-P technique. Syndynes and synchrones, which act as a guide to the modeling, are overlaid. (Note that the January image was obtained when the Earth was crossing the comet's orbital plane, so the syndynes and synchrones overlap along the lie of sight.) Synchrones (solid lines) start at –900 days relative to perihelion, with steps of 100 days. Syndynes (dotted lines) represent particles of radius 1, 3, 10, 30, 100, 300 and 1000 μm. North is up , East is left and the projected sunward direction is noted. Bottom Row: Model contours from the F-P simulations (red), compared to the contours for the corresponding HST images. The basic structure is matched well enough to constrain the dust properties that are needed for our hazard analyses.

Results from the tail modeling are shown in the lower panels of Figure 3, with contours for the models overplotted on the contours for the images. The basic morphologic structure matches well, though some of the details still differ. These deviations are likely due to the simplifying assumptions that are made to avoid making the modeling too unwieldy. However, we note that matching the basic morphology is sufficient for determining the properties that we need.

Results from the full tail model are fairly consistent with the individual results discussed earlier, with some minor variations. The particle size distribution derived from these models is $dn/da \sim a^{-4}$, which suggests that Siding Spring has a fairly typical dust environment. The dust production rates follow a similar trend as that shown in Figure 1, with a rapid increase from >8 AU to ~5 AU, and then a fairly constant level of activity through the observation times. Any significant emission that is added at ~10 AU fills in portions of the tail where little dust is seen, which provides additional evidence that Siding Spring did not become active until after 10 AU. Given the production rates and particle size distribution, we compute a dust mass rate ~15-18 kg/sec. This is again consistent with previous estimates.

The velocity derived from the models follows the function $v \sim 300\ a^{-0.6}\ r_h^{-1.5}$ m/s, which is consistent with the velocities derived from the standoff distance. For comparative purposes, we compute our reference velocity, v_{ref} = 0.42 m/sec for a 1 mm grain at 5 AU. These velocities are somewhat low in comparison to some hydrodynamic models, but they are derived directly from observations of the comet, and are consistent through the various analyses. Furthermore, as will be seen later, the HST observations were obtained during the window of time when the dust being emitted is most likely to reach Mars, and thus the velocities are a good representation of what should be included in the simulations.

For our hazard simulations, we define a nominal case for the velocity, as derived from the observations and perform simulations for that case. However, because the velocity is such a critical parameter, we will also test some more extreme, yet plausible scenarios, to determine if they raise other potential problems.

2.9 Nominal Siding Spring Model

The results from all of our analyses suggest that comet Siding Spring is fairly typical for a dynamically new comet, in that its onset of early activity was rapid and then leveled off . Its behavior is very similar to that of comet ISON (another recent dynamically new comet). For purposes of our hazard analysis, we developed a nominal model that matches the observations and can be used to project the comet's activity backward and forward in time to simulate the conditions that will be present during the Mars close approach. The properties that we adopt for our nominal model are:

1) *General activity*: Onset of activity occurs around 10 AU, and ramps up with a heliocentric distance dependence r_h^{-7} until 6 AU. Inside of 6 AU, the activity remains constant.

2) *Gas and dust production*: CO_2 drives the activity from 10 to 3 AU. CO_2 production was 30 kg/sec in early 2014 (during the constant part of the activity). For a dust-to-gas ratio of 1, the dust production rate is 30 kg/sec. As of March 2014, water and dust production rates inside of 3 AU are unknown, but as discussed below, the most hazardous dust is being emitted outside of this distance.

3) *Dust grain sizes*: Minimum size is 0.1 μm and maximum size is 1 cm (radius).

4) *Particle size distribution*: The particle size distribution varies as a^{-4}.

5) *Emission velocity*: Velocities follow the relation $v \sim 300\ a^{-0.6}\ r_h^{-1.5}$ m/s.

3 Dust Hazard Analysis

Using our model comet parameters, we can project the comet's activity forward in time to simulate what the dust environment will be when the comet passes Mars. The dynamic model used to determine the structure of the coma and tail follows the same principles outlined above, where the dust motions are governed by solar gravity and solar radiation pressure. For this study we use the JPL ephemeris solution #46, which was identified as the best Siding Spring orbit solution to date, and provides a uniform geometry for comparison of the different studies.

We performed simulations with several different velocity dependencies, starting with our nominal case, and then exploring more extreme cases to determine whether they produce conditions that should be investigated further

3.1 Dust Dynamics

The comet's dust environment at the time of the Mars encounter is simulated with the dynamical model of Kelley (2006). In order to reduce the required computational time, we modified the model to use the two-body (Keplerian) propagation functions from NASA's Navigation and Ancillary Information Facility SPICE toolkit. Dust grains are parameterized by the parameter β, which is the ratio of the force from solar radiation pressure to the force from solar gravity. For spherical grains, this ratio reduces to $\beta = 5.7\times10^{-5}\, Q_{pr}/\rho a$, where Q_{pr} is the radiation pressure efficiency, ρ is the grain density, and a is the grain radius (Burns et al. 1979). For grain parameters (Q_{pr}=1, ρ=1000 kg/m^3), a simple conversion from grain radius to β takes the form: a[μm] = 0.57/β.

We performed some simple tests to determine the effects of neglecting planetary perturbations. By comparing zero-ejection velocity syndynes, generated using the Keplerian solution to those generated using the original code (including all planets plus Pluto) reveals the magnitude of planetary perturbation influences. For grains ejected up to 4 years before closest approach, syndynes for β ≤ 0.001 are consistent with the original code to within 500 km, which is well within the orbital solution uncertainties. For β ≤ 0.01 the error increases to ~4000 km, but this is the uncertainty on a position that has moved ~10^7 km from the nucleus, and thus is too far away to be relevant to our hazard analysis. We also considered whether gravitational focusing by Mars could significantly alter the dust trajectories or velocities at encounter. Ignoring the Martian atmosphere, particles grazing the planet's surface are displaced <100 km at closest approach, their trajectories are deflected by less than 0.5°, and they are accelerated by less than 1%. Thus, the Keplerian solution is sufficient for our purposes.

3.2 Reference Frames

Simulations are performed in the ecliptic J2000 reference frame. To facilitate our investigation of the hazards at Mars, we transform the results to a coordinate system defined relative to the geometry at close approach. For this "close approach frame", the origin is located at the nucleus, the X-axis is defined by the comet-Mars position vector at the time of closest approach, and the Y-axis is parallel to the comet-Mars velocity vector (also at the closest approach, and thus perpendicular to the position vector). The Z-axis completes the right-hand reference frame.

We can also translate the positions along the X axis into a Mars-centered reference frame, for simplicity in analyzing the dust hazard. With this frame, the X-Z coordinates define a grain's position relative to Mars, and the relative timing of its arrival is defined by its Y-axis coordinate (55.96 km represents an offset of 1 second from the time of close approach, 10^5 km corresponds to ~29.8 min).

3.3 Dust Coma Simulations

Our basic simulation is generated from a wide range of particle parameters, and can be used to understand exactly what combination of particle size, ejection speed, and ejection time is needed to generate impacts at Mars. It consists of 10^9 particles selected from the following parameters: ages range uniformly from 0 to 4~yr (emission out to r_h=13 AU); expansion speeds range uniformly from 0 to v_{ref} a[mm]$^{-0.5}$ (r_h/5 AU)$^{-1}$, where v_{ref} =1.9 m/sec. This range brackets the velocities described in our nominal comet model. Ejection velocities are radial and isotropically distributed around the nucleus. Grain radii are selected from a distribution uniform in log-space ($dn/d\log a \propto 1$) ranging from 10 to 10^4 μm. The logarithmic distribution in radius ensures our final results will have a good statistical representation of each size decade. At the end of the run we must account for the overrepresentation of large grains, so we weight each particle in the simulation by its occurrence in the size distribution to provide a real estimate of each grain's frequency of occurrence in the comet's coma.

Given our measurements of the comet's grain size distribution, grain ejection speeds, and dust production rate history, we define our nominal comet model as parameter set A in Table II. From our simulation of 10^9 particles, we select only those that match the ejection speed criteria of set A, and compute the impact hazard accordingly.

Deviations from parameter set A will be used to estimate the uncertainties in our model, and compute an upper-limit grain fluence at Mars. To that end, parameter set B adopts theoretical dust velocities (e.g. Crifo & Rodionov 1997), which are slightly higher than those measured in Siding Spring, and parameter set C that keeps the dust parameters from set B, but also shifts the comet's close approach distance closer to Mars, to investigate how the orbital uncertainties (5000 km 3σ) might affect the hazard analysis.

A final parameter set, labeled D, investigates the velocity conditions discussed in Section 2.6, where $v \sim 600\ r_h^{-2}$ m/s (which gives a reference velocity, v_{ref} = 0.76 m/sec). These velocities exceed the bounds of the original simulation for heliocentric distances closer to the Mars encounter. Therefore, we generated a second simulation of 10^9 particles, with speeds picked uniformly from 0 to 1.9 a[mm]$^{-0.5}$ (r_h/5 AU)$^{-2}$ m/s. This velocity range brackets the conditions proposed in parameter set D, and the simulation can be reused if in the future an even higher scenario is warranted. Although the bulk of the dust in the coma and tail does not follow parameter set D's velocity law, this case does address any fast moving grains not accounted for in the nominal comet model.

Details regarding the parameter sets for each of the simulations is summarized in Table II.

3.4 Impact Criteria

For our statistical purposes, we define an impact as any particle found within 10,000 km of the center of Mars. This distance includes the orbit of Phobos (9400 km semi-major axis), and the apoapsis of the MAVEN spacecraft's nominal science orbit (6000 km). We also investigate a second 5000 km region centered on the position of Deimos (2.3×10^4 km semi-major axis) at the time of closest approach. A third region of interest is

based on the apoapsis position of the MAVEN spacecraft, based on the orbit that includes a 5-week delay in science operations (apoapsis of 48,000 km).

Table II. Dust Simulation Parameters

Parameter	Set A	Set B	Set C	Set D
Gas production rate at 3.8 AU, Q_g (kg/s)	30			
Q_g heliocentric dependence for $r_h \leq 6.1$ AU	r_h^0			
Q_g heliocentric dependence for $r_h \geq 6.1$ AU	r_h^{-7}			
Dust-to-gas mass ratio	1.0			
Reference expansion speed [a] v_{ref} (m/sec)	0.42	0.71	0.71	0.76
Expansion speed dependence on a	$a^{-0.6}$	$a^{-0.5}$	$a^{-0.5}$	$a^{-0.5}$
Expansion speed dependence on r_h	$r_h^{-1.5}$	$r_h^{-1.0}$	$r_h^{-1.0}$	$r_h^{-2.0}$
Minimum grain radius a_{min} (μm)	0.1			
Maximum grain radius a_{max} (μm)	10^4			
Grain size distribution dn/da	a^{-4}			
Comet-Mars closest-approach distance (km)	1.35×10^5		1.30×10^5	
Raw (unweighted) number of particles [b]	5.9×10^5		7.7×10^5	8.4×10^3

Empty cells indicate the parameter is the same as for the nominal case in Set A

[a] Expansion speed of 1 mm-radius grains at 5 AU. A tolerance of ±5% is allowed for each parameter set.

[b] After removing particles that do not meet the ejection speed criteria

3.5 Simulation Results – Nominal Comet Model

The simulation for our nominal comet model (parameter set A) produces no impacts. This result suggests that, given our current understanding of comet Siding Spring, its dust coma and tail will present no hazard to the spacecraft around Mars.

Although this result is good news for the spacecraft hazard, it provides no quantitative information that can be used for statistical analyses or for evaluation of the spacecraft hazard. Thus, we ran our additional simulations with more extreme conditions, to determine some upper limits on the fluences. These additional models are not out of line with the observational data, so they do represent credible conditions that should be considered, especially since the changes do create conditions where impacts occur.

3.6 Impact Hazard

The spatial distribution of all 10^9 particles in our $v \sim r_h^{-1}$ simulation is shown, with respect to the path of Mars at closest approach, in the first column of Figure 4. It is clear that Mars passes through the outer edge of the coma envelope, producing impacts on the planet. This raw simulation, which is unconstrained by the observed comet parameters, provides a guide to understanding what combination of grain size, ejection velocity, and age, produce impacts at Mars. The particles within parameter sets A and B are subsets of this raw simulation, as constrained by the observations of the comet. The spatial distributions of grains for cases A and B are shown in the next two columns. (Set C is not shown, since it is simply an offset of set B). Set D, shown in the last column of Figure 4, is a subset of a separate simulation, with $v \sim r_h^{-2}$.

Figure 5 shows the relevant grain parameters for the particles from the raw simulation that yield impacts. The only particles in our r_h^{-1} simulation that reach the

Martian system are those ejected with speeds of a few meters per second, have radii of 0.7-3.6 mm, and are ejected at least 1.5 yr prior to the encounter.

We also note that for the high velocity at low heliocentric distance case (parameter set D) scenario, we again see no impacts. This confirms that the comet's activity inside of 3 AU is essentially irrelevant to the dust hazard at Mars.

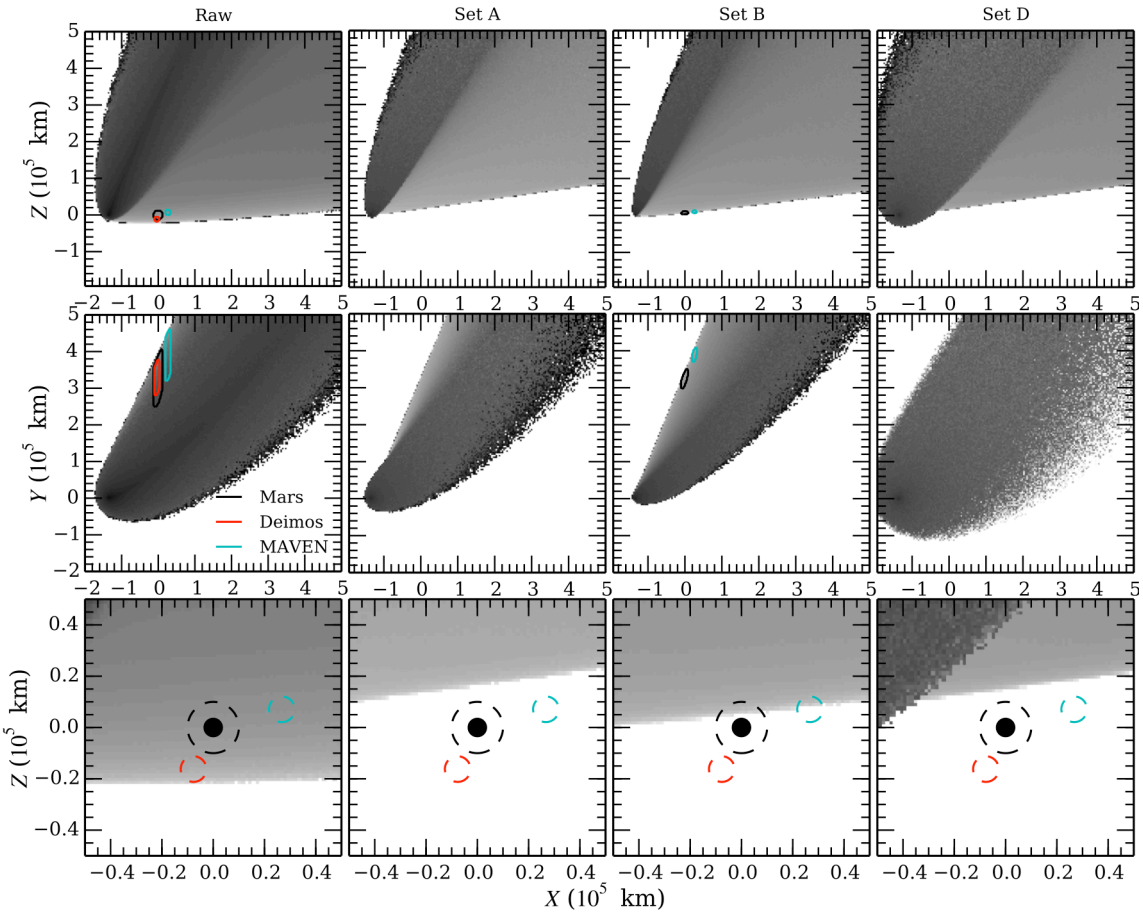

Figure 4. Distribution of comet dust based on our simulations and rotated into our closest approach reference frame. The top row shows the view looking along Mars' path, and the second row shows the view from above the path. The bottom row zooms in on the region around Mars from the top row. The solid black circle is Mars' profile, with the dashed circle representing our 10,000 km impact circle (discussed in the text). The red and blue circles represent 5,000 km impact zones around Deimos and the apoapse position of MAVEN at closest approach. Column labels indicate the dust being plotted: Raw—all 10^9 particles in our first simulation, which was an unconstrained exploration of ejection speed and other dust properties; Set A/B/D—particles that correspond to our parameter sets A/B/D, as listed in Table III. Note that parameter set C (not shown) is the same as B, but with the dust offset toward Mars according to its 3-σ position uncertainty. All particles have been weighted to reflect a size distribution (at the nucleus) of $dn/da \propto a^{-4}$. No other scaling has been applied (e.g., dust production rate).

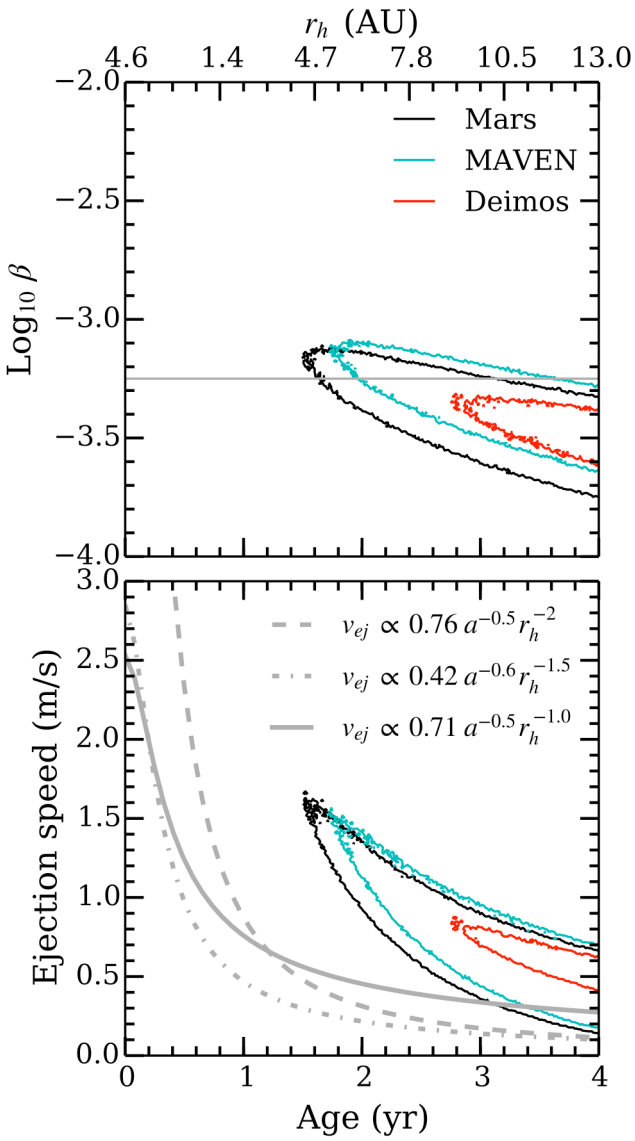

Figure 5. The relationship between β, age, and ejection speed of particles from our raw simulation that are found to impact the Mars, Deimos, and MAVEN regions. The envelope for each target outlines the property range of potential impactors. The top panel indicates that only particles between 0.7 to 3.6 mm (the horizontal line denotes 1mm), and older than 1.5 years can reach Mars. The bottom panel shows ejection speeds are low and depend on the particle's age. The different curves show the ejection speeds of a 1 mm grain for each of the velocity distributions considered.

For each parameter set, the impact hazards are computed by taking the set of particles found in each region of interest, removing those that are outside our chosen ejection speed range, and weighting each particle for the chosen parameter set (including corrections for the simulation's particle size distribution bias). Table III lists the impact fluences for Mars, and the beginning and end times (UTC at Mars) of the hazard. As noted above, no impacts are expected for our nominal comet model, even if the velocities at

small r_h are high. For these comet models, the ejection speeds of dust grains emitted beyond 3 AU are too low to place particles within the vicinity of Mars (Figure 5). Even displacing the comet dust in these two models according to the 3-σ uncertainty ellipse of the orbit does not result in any impacts.

Table III. Simulation Results

Parameter	Set A	Set B	Set C	Set D
Raw (unweighted) number of impacting grains [a]	0	4.5×10^3	1.5×10^4	0
Total fluence [a,b] (10^{-7} grains/m^2)	0	1.14±0.02	3.91±0.03	0
Total fluence [a,b] (10^{-12} kg/m^2)	0	3.27±0.05	11.7±0.1	0
Time of impacts [a] (UTC hr)	-	19:57-20:17	19:52-20:11	-

[a] After removing particles that do not meet the ejection speed criteria
[b] Total fluence and impact times are given for Mars. Times were calculated using 5 min bins. Fluence uncertainties are based on Poisson statistics, given the number of particles found near Mars.

In order to attain impacting trajectories, the grains ejected at r_h>3 AU need higher ejection speeds than we find in our nominal comet model. This requirement is accomplished with the size-r_h-speed relationship of parameter set B: $v \propto a^{-0.5}\ r_h^{-1}$. However, even in this case, the total number of impacting grains remains low, with only 1×10^{-7} grains/m^2. The grains arrive 88 to 108 min after the comet's closest approach, based on the comet's current predicted closest approach time. This confirms that the greatest hazard occurs when Mars is closest to the comet's orbital track. Note that although the present ephemeris solution for the nucleus is ballistic (i.e., it does not include non-gravitational forces), non-gravitational forces will not affect arrival time of the dust because the dust is ejected at heliocentric distances where the activity of the comet (and resulting non-gravitational forces) is low. However, the current nucleus ephemeris uncertainty is still valid for the dust. Displacing the dust in parameter set B closer to Mars (set C), has the effect of shifting the arrival time 5 min earlier, and increasing the fluence by a factor of 4.

The fluence results are summarized for Mars and MAVEN in Figure 6. Grains near these objects are limited to the size range 1 to 3 mm in radius. The timing of the hazard at MAVEN's distant apoapsis is 25 min later than the hazard at Mars, and the fluences are a factor of 2 higher.

Overall, we do not expect any impacts on Mars-orbiting spacecraft. Based on the cross-sectional area of Mars, and our 10,000~km average fluence for our worst-case scenario, the planet may receive up to 10^7 impacts from 1- to 3-mm-radius grains, totaling ~100 kg, based on our models. Few impacts are expected on Phobos (<100), and no impacts at Deimos.

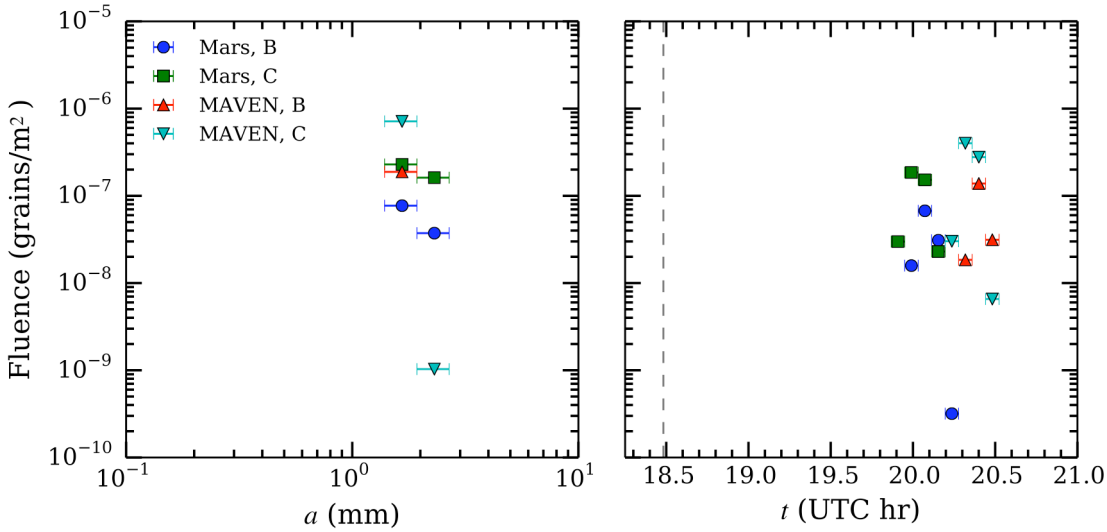

Figure 6. Left panel: Dust grain fluences in our regions of interest versus grain radius, computed for parameter sets B and C (sets A and D have no impacts). Error bars indicate the bin width over which the flux was summed. Right panel: Fluence versus time, in 5-min bins.

4 Comparison with Other Results

Moorhead et al. (2013) and Vaubaillon et al (2014) predict significantly larger impact hazards, with fluences of 0.1 grains/m^2 and larger. Their large fluences appear to primarily be due to their choice in dust ejection speeds. Moorhead et al. adopted a velocity profile from Brown & Jones (1998), and a low-density (0.1 g/cm^3) particle, that produces a reference velocity of 36 m/sec. Accounting for the different assumptions in densities by scaling v_{ref} with $(1.0/0.1)^{1/2}$ results in expansion speeds more than an order of magnitude above our worst-case model (v_{ref}=11 m/s versus 0.71 m/s). Vaubaillon et al. (2014) used the Crifo and Rodionov (1997) model, but assumed a large nucleus that produced very high velocities (Vaubaillon, personal communication). Their models only consider activity inside of 3 AU, but the velocity of a 1 mm grain begins around 50 m/sec, and increases to several hundred m/sec around the time of the Mars encounter. Smaller grains have even higher velocities. This has the effect of producing a dust coma millions of km across, which produces a massive number of impacts. We note that neither Moorhead et al. nor Vaubaillon et al. used any observations to constrain their velocity models.

In contrast, Ye & Hui (2014) used ground-based observations of Siding Spring and the similarly bright comet C/2012 S1 (ISON) to derive a size-r_h-speed relationship, and obtained results more consistent with ours. They found v=2.9 [m/sec] $(a/5\ \text{mm})^{-0.5}\ r_h^{-1}$ best matched their data, assuming a nucleus of 2.5-km radius and 0.3 g/cm^3 density dust. These parameters resulted in no impacts for a>0.1 mm. In our parameterization, these speeds correspond to v_{ref} = 1.3 m/sec, which is higher even than our worst-case scenario model (set B) by a factor of 1.8. When they include smaller dust grains, down to 10 μm in radius, they find impacts at Mars spanning 19:20 to 20:45 UTC with a total fluence of

2.6×10^{-6} grains/m^2. Using their speeds and our production rate history, we find the same fluence, but unlike Ye & Hui (2014), all impacts are millimeter sized.

Acknowledgements

Support for this work was provided by NASA Jet Propulsion Laboratory's Mars Critical Data Products Program.

The simulations presented in this paper were carried out using a computing cluster administered by the Center for Theory and Computation of the Department of Astronomy at the University of Maryland ("YORP").

This research made use of Astropy, a community-developed core Python package for Astronomy.

This work made use of data obtained by the PanSTARRS consortium.

We thank the Swift team for awarding us Director's Discretionary Time to observe comet C/2013 A1 and for the careful and successful planning of these observations.

References

A'Hearn, M. F., Schleicher, D. G., Millis, R. L., Feldman, P. D., & Thompson, D. T. (1984) "Comet Bowell 1980b", *Astron. J.* **89**, 579-591.

Bodewits, D., Farnham, T.L., A'Hearn, M.F., Feaga, L.M., McKay, A., Schleicher, D.G. and Sunshine, J.M. (2014) "The Evolving Activity of the Dynamically Young Comet C/2009 P1 (Garradd)", Astrophys. J. **786**:48.

Burns, J. A., Lamy, P. L. and Soter, S. (1979) "Radiation Forces on Small Particles in the Solar System", *Icarus* **40**, 1-48.

Crifo, J.F., Rodionov, A.V. (1997) "The dependence of the circumnuclear coma structure on the properties of the nucleus" *Icarus* **127**, 319–353.

Crovisier, J. and Encrenaz, T. (1983) "Infrared fluorescence of molecules in comets: the general synthetic spectrum", *A&A* **126**, 170.

Farnham, T.L. (1996) "Modeling Cometary Dust Tails with a Pseudo-Finson-Probstein Technique", PhD Thesis, University of Hawaii at Manoa, Honolulu, HI.

Finson, M. L. and Probstein, R. F. (1968) "A Theory of Dust Comets I. Model and Equations", *Astrophys J.* **154**, 327-354.

Fulle, M. (2004) "Motion of Cometary Dust" in *Comets II* (Michel Festou, H. Uwe Keller and Harold Weaver, eds.) The University of Arizona Press, Tucson. pp. 449-469.

Kelley, M.S. (2006) PhD Thesis, University of Minnesota, Minneapolis, MN.

Meech, K. J., and Svoren, J. (2004) "Using Cometary Activity to Trace the Physical and Chemical Evolution of Cometary Nuclei" in *Comets II* (Michel Festou, H. Uwe Keller and Harold Weaver, eds.) The University of Arizona Press, Tucson. pp. 317-335.

Oort, J. H., Schmidt, M. (1951) "Differences between new and old comets", *Bull. Ast. Inst. Netherlands* **11**, 259.

Ootsubo, T., Kawakita, H., Hamada, S., Kobayashi, H., Yamaguchi, M., Usui, F., Nakagawa, T., Ueno, M, Ihiguro, M., Sekiguchi, T., Watanabe, J. Sakon, I., Shimonishi, T., and Onaka, T. (2012) "AKARI Near-Infrared Spectroscopic Survey for CO2 in 18 Comets", *Astrophys. J.* **752**:15.

Moorhead, A.V., Wiegart, P.A., and Cooke, W.J. (2013) "The meteoroid fluence at Mars due to comet C/2013 A1 (Siding Spring)", *Icarus* **231**, 13.

Tricarico, P., Samarasinha, H.H., Sykes, M.V., Li, J.-Y., Farnham, T.L., Kelley, M.S.P., Farnocchia, D. Stevenson, R., Bauer, J.M., and Lock, R.E. (2014) "Delivery of Dust Grains from Comet C/2013 A1 (Siding Spring) to Mars", in prep.

Vaubaillon, J., Maquet, L. and Soja, R. (2014) "Meteor hurricane at Mars on 2014 October 19 from comet C/2013 A1", MNRAS, doi:10.1093/mnras/stu160.

Whipple, F. L. (1978) "Cometary brightness variation and nucleus structure", *Moon and Planets* **18**, 343-359.

Whipple, F. L. (1951) "A Comet Model. II. Physical Relations for Comets and Meteors", *Astrophys. J.* **113**, 464.

Ye, Q.-Z. and Hui, M.T. (2014) "An Early Look of Comet C/2013 A1 (Siding Spring): Breathtaker or Nightmare?", *Earth and Planetary Astrophysics*, submitted.